Global Fluid Power Society PhD Symposium 2022| Naples, Italy - 2022

Design, Modeling, and Experimental Characterization of a Fast Additively Manufacturable MRI-Compatible Pneumatic Motor for Surgical Robots

Mengtang Li[1,#,*], Jing Zhang[1,#], Xiyun Wu[1], Jieting Yuan[1],

Xiyu Wang[1], Yongyin Ye[1], and Beichen Ding[1]

[1]School of Intelligent Systems Engineering, Sun Yat-Sen University, Shenzhen, China

Email: limt29@mail.sysu.edu.cn

#Contributed Equally

**Corresponding Author*

Abstract.

For robot assisted surgery under magnetic resonance imaging (MRI) guidance, constraints such as material limits, actuation method limits and available sensor limits have made the design and control of an actuation and transmission system the most challenging problem. Aiming at tackling the aforementioned issues, this paper proposes a novel pneumatic powered motor, which features few as two inputs, continuous and back-drivable motion outputs, integrated MRI-compatible speed sensor, compact modularly switchable down-speed components, and fast additively manufacture ability (22 components in total). It promisingly fills the gap between the current MRI-compatible surgical robots and available actuation methods and offers an alternative approach for the community to actuate various surgical robotic platforms. Detailed design methods for the pneumatic motor and integrated rotary encoder are developed first. Motor performances are experimentally evaluated next to analyse and demonstrate its characteristics under various pressures against different load torques. Finally, the proposed pneumatic motor is compared with recent MRI-compatible pneumatic actuators, illustrating the feasibility of the proposed fluid power motor for actuations of MRI surgical robots.

Keywords. Pneumatic systems, Pumps and motors, Fluid power components, Fluid power drives and transmissions, MRI (Magnetic Resonance Imaging)

1. INTRODUCTION

Compared with computed tomography (CT) and X-ray, magnetic resonance imaging technology can quickly and clearly generate human soft tissue imaging without exposing patients or physicians to ionizing radiation. These advantages make MRI guided surgical robot an appealing trend in the future of minimal invasive surgery [1]. However, the magnetic environment strictly restricts the medical devices constructed of ferromagnetic materials and other specific materials from entering the magnetic scanner to prevent danger or degrade the imaging quality. The American Society for Testing and Materials (ASTM) [2] and the U.S. Food and Drug Administration (FDA) [3] have strictly defined standards for MR-compatible and MR-safe materials and driving methods. Considering the safety and imaging quality requirements, the design and construction of MR-compatible actuators are the foundation and critical technology of MRI guided surgical robot [4].

On the premise of MRI compatible materials, pneumatic actuators demonstrate noteworthy advantages in compact size, simpler structure, sterility and safety, compared with other actuation methods, such as hydraulics [5,6,7], shape memory alloy (SMA) [8], piezoelectric ceramics motor (also known as ultrasonic motor) [9,10], tendon (cable) drive [11,12], etc. Hence it is the most widely studied and applied actuation methods in the field of MRI guided surgical robot [13,14]. Among pneumatic methods, the turbine/fan-based air motor [15,16] illustrates attracting advantages in manufacturing simplicity and device compactness compared with the piston cylinder-based actuator [17,18,19]. It also has advantages in generating continuous and bidirectional motions compared with gear-based pneumatic stepper actuator that can only output unidirectional rotary motion with fixed steps [20,21,22,23]. A novel flexible fluidic actuator (FFA) for MRI surgical robots can dramatically simplify the manufacture progress via selective laser sintering (SLS) [24], yet it suffers from the same issues as the gear-based pneumatic actuators and is only able to produce step motions slowly. It can be seen that the pneumatic motor acts like a ‘DC motor’ for the joints of MRI guided surgical robots. However, only one design of MRI compatible pneumatic rotary motor has been designed and applied into surgical robot platforms according to a comprehensive literature review done in 2020 [4]. Adequate room for design improvement exists.

This paper proposes a new MRI compatible pneumatic motor based on strain wave harmonic mechanism, featuring the characteristics of 1) continuous and back-drivable motion outputs, 2) integrated MRI-compatible speed sensor, 3) compact modularly switchable down-speed components, and 4) fast additively manufacture ability. Preliminary motor performance tests are conducted to evaluate and analyze the design and working principle. The proposed actuator aims at offering the community with a new actuation method for the community to actuate various surgical robotic platforms. The remainder of this paper arranges as follows. Section 2 presents the mechanism design and working principle, and integrated rotary encoder. Section 3 describes the motor performance characterizations. Results discussion and actuator comparison are included as well. Section 4 draws conclusive remarks.

2. MATERIALS AND METHODS

2.1. Mechanism Design and Working Principle

The proposed MRI compatible pneumatic motor for surgical robots mainly consists a turbine and a strain wave gear box (also called harmonic drive) with necessary supporting cases. The turbine and all supporting cases are fast additively manufactured by a 3D printer using acrylonitrile butadiene styrene (ABS). Other MRI-compatible materials can also be used to improve the structure strength or to reduce motion friction. The proposed pneumatic motor differs from the conventional ones which adopt fix displacement architectures for example a sliding vane structure. A modified Pelton turbine [25] is designed and utilized to allow bidirectional operation when pressurized air is supplied to the two inlet ports through long transmission air hoses from a standard medical gas tank placed in the safe room. The pressurized air pushes the turbine to rotate and dissipates from exhaust ports into the ambient environment, without any safety or sterility concerns. Necessary ball bearings are placed axially to support the shaft with low rotary frictions.

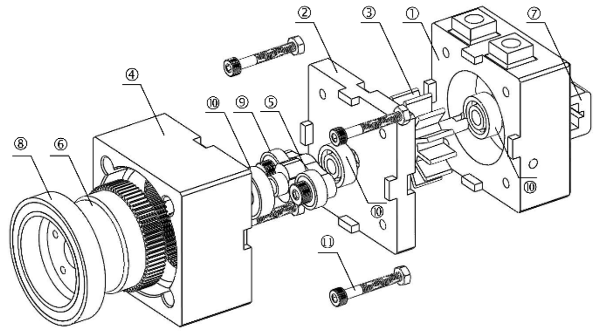

Figure 1 Exploded CAD view of the pneumatic motor assembly.

A harmonic drive system couples with the output shaft of the turbine to increase output torque while reducing speed. The circular spline is incorporated into the harmonic drive case. The flex spline is fabricated with soft material (thermplastic polyurethane, TPU) to permit some deformation. The wave generator is designed to install two ball bearings distributed evenly. As the wave generator rotates along with the turbine shaft, the outer cases of the two ball bearings push against and roll on the inner surface the deformable flex spine, causing the flex spline to rotate in the opposite direction at a reduced speed. The flex spine meshes with the circular spline, outputting torque for joints of surgical robots. A reduction ratio r can be obtained by the following equation:

$$r = \frac{n_{flex} - n_{cir}}{n_{flex}} \tag{1}$$

where n_{flex} and n_{cir} are the number of teeth of flex spline and circular spline, respectively. Normally, the circular spline involves two more teeth than the flex spline, leading to the result of:

$$r = \frac{-2}{n_{flex}} < 0 \tag{2}$$

Hence, the mechanism of the strain wave gear is capable of achieving a large down-gear ratio within a compact space. The negative sign tells the fact the output rotation is in the opposite with the input shaft. The detailed design of a first-generation prototype (60mm x 40mm x 40mm) is depicted in Figure 1, along with part descriptions listed in Table 1. Photographs of the first-generation prototype is shown in Figure 2. The working principle of the soft flex spline is demonstrated as well. Here a harmonic drive system with -1:40 gear ratio is designed. Other options can also be customed designed.

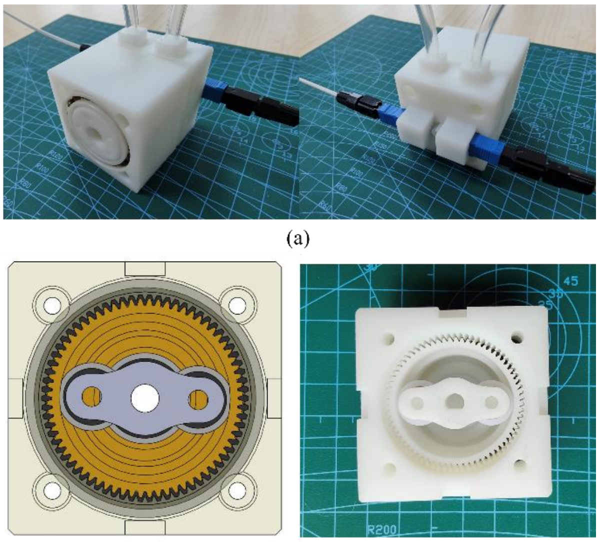

(a)

(b) (c)

Figure 2 (a) Assembly of the proposed pneumatic motor. (b) CAD view of the strain wave gear system: the flex spline is designed in a circular manner (not deformed here). (c) Photo of the strain wave gear system: the flex spline is deformed because the two ball bearings push against it.

Table 1 Fabrication materials of the proposed pneumatic motor

Number	Part Name	Description	Material
1	Motor case 1	3D print	ABS
2	Motor case 2	3D print	ABS
3	Turbine	3D print	ABS
4	Circular spline	3D print	ABS
5	Wave generator	3D print	ABS
6	Flex spline	3D print	TPU-30
7	Rotary encoder (not plotted)	Internet fiber wire and wire connector	Optical fiber and plastic
8	Ball bearing 1	KIF®Φ30×Φ42×7	Polyamide and glass
9	Ball bearing 2	KIF®Φ4×Φ12×4	Polyamide and glass
10	Ball bearing 3	KIF®Φ5×Φ16×5	Polyamide and glass
11	Screws and Nuts	M3×252	Plastic

2.2. Integrated Rotary Encoder

Conventional rotary encoder relies on electrical signal to function and transmit measurement data, which inevitably involves danger inside the scanner and compromises MR imaging quality. Hence, an MRI compatible rotary encoder is necessarily needed. Inspired by the built-in encoder design in [16], two Internet optical fiber wires are used where one fiber carries a continuous light beam generated from a light source (e.g. a fiber wire visual fault locator, Cinyobo®) while the other one receives the light beam. A cutout at the end of the shaft cyclically blocks the light beam when the shaft rotates, thus creating two binary pulses per revolution. The pulses of high/low light density can be captured by a photoresistor, transmitting the binary signal into useful rotary speed data. Another pair of optical fiber wires at $90\,deg$ angular offset can be added to increase the resolution and accuracy at the cost of a larger device size. The shaft speed $n\ [rpm]$ during a period of time $T\ [sec]$ can simply be obtained by:

$$n = \frac{n_{pulse}}{2T} \cdot \frac{1}{n_{optpair}} \cdot \frac{60sec}{1min} \tag{3}$$

where n_{pulse} is the number of pulses, $n_{optpair}$ is the number of optical fiber wire pairs. Introducing interrupts every time a high pulse comes and computing the time interval between each interrupt is another method to obtain instantaneous rotary speed and can significantly improve the accuracy. But methods similar to this would require higher sampling frequency.

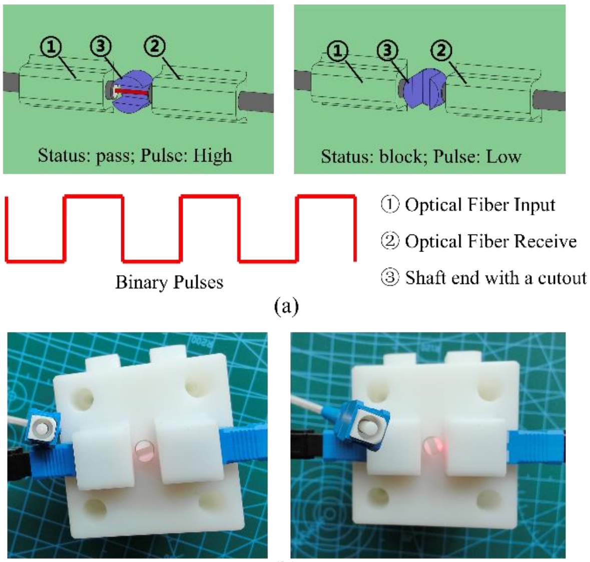

(a)

(b)

Figure 3 (a) Schematics of the integrated rotary encoder: Left: continuous light beam can pass through the cutout of the end of the shaft, leading to high light density; Right: light is blocked, resulting in low light density. (b) Photos of optical light beam passes (left) or is blocked (right).

Consider the fragility of optical fibers (the core of an optical fiber wire made of glass), and the potential miscounting due to misalignment of optical fiber wires, this paper improves the previous design by utilizing standard Internet optical fiber wire connectors. This not only protects the light transmitting optical fibers, but also provides pre-aligned click-on/off sockets. Figure 3 shows the detailed design and working principle of the integrated rotary encoder.

2.3. *Minimally Invasive Steerable Needle Robot*

The proposed MRI-compatible pneumatic motor serves as a fundamental power unit for joints of surgical robots. To straightforwardly illustrate the potential applications of the proposed motor, a minimally invasive steerable needle deployment robot, which can be used for percutaneous treatment for biopsy or delivered therapy, is shown in Figure 4.

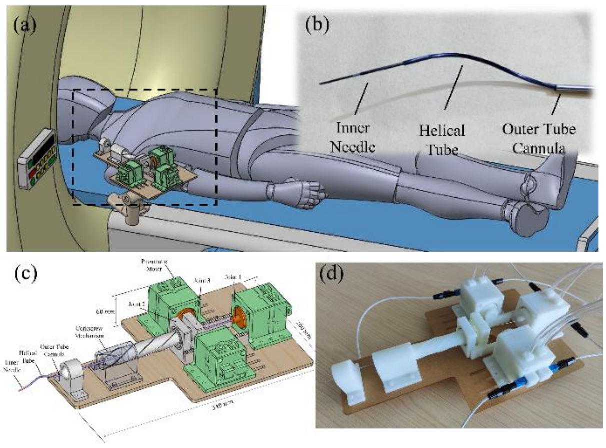

Figure 4 (a) Schematic diagram of an MRI-compatible steerable needle robot actuated by the proposed motor. (b) A minimally invasive concentric steerable needle. (c) Design details of the needle deployment robot. (d) Photo of the first-generation prototype.

3. RESULTS

3.1. *Motor Performance Evaluation*

An experimental prototype of the proposed MRI compatible motor is designed and fast manufactured to study its working mechanism and performance. The integrated rotary encoder is first tested to evaluate its performance accuracy by comparing the calculated speed with measurements from a commercial handheld laser tachometer (FEITA). Different pressures are supplied to the proposed motor, leading to different rotary speeds. Since a long polyurethane transmission air hose (1 m, I.D. 4mm, O.D. 6mm) is used, pressure delay and hence motor response delay are inevitable, which also occurs in the real MRI compatible pneumatic surgical robots [26]. Here, rotary speed is read once the motor reaches its steady state. Figure 5 plots and compares the rotary speed (without strain wave gear system) measurements from the integrated encoder and the commercial tachometer at various shaft speeds. It can be seen that both signals match well and errors for speeds higher than $300\ [rpm]$ in between falls below 2%. The large error at low speed comes from light pulse miscounting and this affects significantly at lower speeds. Since gear-down component exists and the motor normally operates at middle to high speed, the miscounting would affect less and hence the accuracy of the proposed encoder is sufficient.

Next, the output shaft of the prototype is attached to a magnetic particle brake (SKISIA PMB-0.5, 0.5 Nm max) to simulate various resistive load torques. The input pressure is manually altered by a throttle valve, and pressure level is measured by a pressure transducer (LONTROL, 0-0.6 MPa, 4-20 mA) placed right next to the motor. Under a certain level of

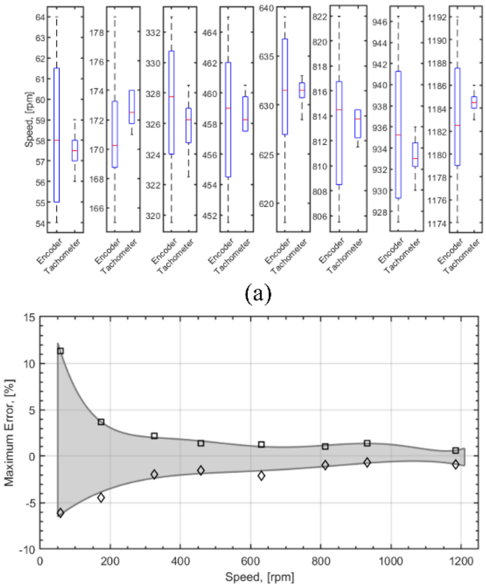

(a)

(b)

Figure 5 Encoder accuracy. (a) Encoder measurements vs tachometer measurements [rpm]. (b) Error bounds from 8 trails for each test speed [%].

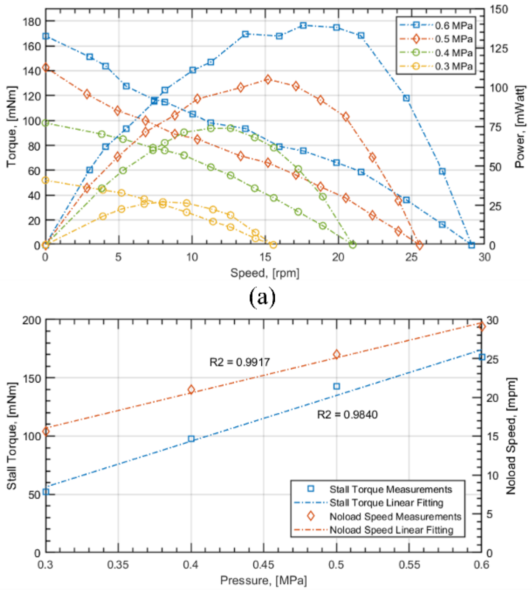

(a)

(b)

Figure 6 (a) Left y-axis: Torque vs speed under different pressures. Right y-axis: Corresponding power vs speed under different pressures. (b) Stall torque and no-load speed with respect to various input pressure.

input pneumatic pressure, the resistive load torque is gradually increased from zero until the stall torque. A steady rotary speed is eventually reached under a certain load torque and input pressure, reflecting the speed versus torque characteristics.

The resulting motor performance characteristics are plotted in Figure 6(a). The left y-axis shows different torque versus rotary speed under various supplied pressure, while the right one shows the corresponding output motor power calculated by $P = \omega\tau$. Clear parabolic shapes are noticed in the plot, where maximum power or optimal operation condition lies in the middle-to-high speed region. Dynamic models of the pneumatic motor can be characterized and fitted using the acquired empirical data. However, since surgical operations are slow and steady, only low bandwidth motions (<0.5~1Hz) are needed [26]. Therefore, satisfactory accuracy can still be achieved with model-independent simple PI control using feedback provided by integrated rotary encoder.

Intersections of these characteristic curves with x-axis and y-axis show the stall torque and no-load speed versus different input pressure, which are more straightforwardly plotted in the left and right y-axes of Figure 6(b), respectively. It can be seen that the motor speed and torque have a fairly linear relationships with input pressure (R^2>0.98). The slope also relies on the gear ratios.

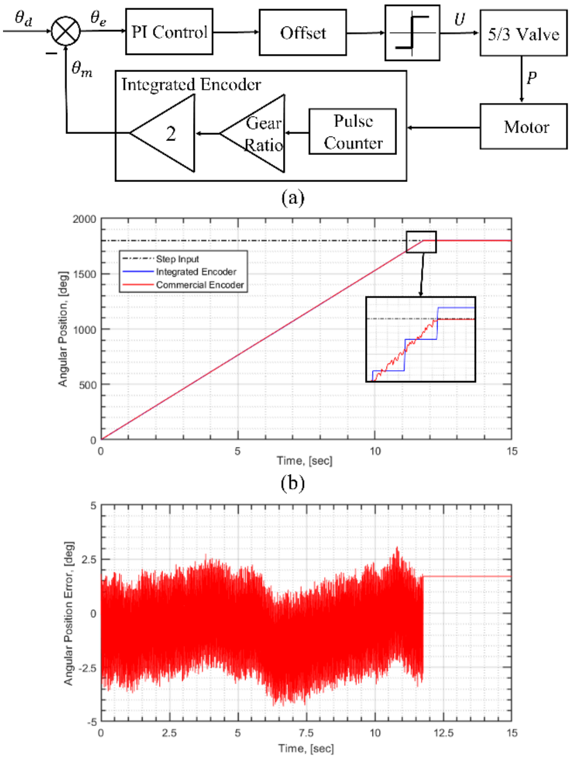

Figure 7 (a) Control diagram. (b) Angular position step response [deg]. (c) Error between the integrated encoder and a commercial rotary encoder [deg].

3.2. Motor Control Performance

A closed-loop control test is conducted to further evaluate the proposed motor with its integrated rotary encoder. A step input of $10\pi\, rad$ (five revolutions, output shaft rotary angle) is sent as a set point to the pneumatic motor. The integrated encoder counts the pulses to acquire the rotated angle. A command voltage is generated by a simple PI controller with angular position error as the input. Since a basin-like relationship between the input electrical signal (it is more obvious for voltage command than current command) and the pneumatic conductance around the center exists for conventional 5/3 directional proportional solenoid pneumatic valves, an offset is established (positive 5 Volts here). The supplied air pressure is set to 0.5 MPa. An absolute optical rotary encoder (HKT32) is used to compare with the integrated encoder and the results are plotted out in Figure 7.

Generally, the two signal matches fairly well except that some discrepancy occurs at the end region. This can be explained by the fact that one input shaft revolution only generates two pulses and 80 pulses for each output shaft revolution, leading to a $4.5\, deg$ resolution. Also, note that this simple control strategy works because a dead band caused by the gear system's frictions can halt the rotor fast enough once the supplied pressured is stopped, which is similar to other turbine or gear-based MRI compatible pneumatic actuators.

3.3. Comparative Study

The proposed motor is compared with some representative MRI compatible pneumatic actuators in the aspects of size, manufacture complexity, dynamic performance, integrated encoder, and bi-directional motion ability, listed in Table 2. A comprehensive comparison among recent MRI compatible actuators including pneumatics, hydraulics, SMA, piezo motor and other novel methods can be found in [4].

Table 2 MRI compatible motor comparison

	Stoianovici et al. [22]	Sajima et al. [20]	Chen et al [21]	Chen et al [16]	Proposed
Mechanism	Pneumatics, gear	Pneumatics, gear	Pneumatics, gear	Pneumatics, turbine	Pneumatics, turbine
Number of parts	~25	~10	~7	~30*	20**
Size [mm]	Φ85×30	Φ30×35	Φ10×60	Φ44×79	60×40×40
Speed [rpm]	166.6	50	60	370	29
Torque [mNm]	640	150	90	460	170
Power [W]	3	0.47	2.4	6	0.14
Encoder	Yes	No	No	Yes	Yes
Bi-directional	No	No	No	Yes	Yes

*Every piece of all the Tamiya® planetary gear boxes is counted.

**Including all screws and nuts.

The proposed MRI compatible pneumatic motor is inspired by the needs of improving the previous design (Chen's Pneumatic Motor [16], developed by the author's former group). It can be seen that the proposed pneumatic motor consists relatively fewer components due to the usage of the strain wave gear mechanism. Compared with Chen's Motor [16], the proposed pneumatic motor is manufacturable through fast additively manufacture and standard mechanical components, eliminating dependencies on purchasing Tamiya® No. 72001 for the (four) planetary gear box. Though these planetary gear boxes can be 3D printed, it involves more components than the proposed design, leading to higher structure complexity. Also, since it falls into the pneumatic turbine based actuator category, it is capable of generating continuous bi-directional motion, serving as a more flexible surgical robot joint.

Yet, note that the output speed and torque of the proposed pneumatic motor prototype are comparatively low with other actuators. This may be explained by the fact that 1) the friction between the rolling ball bearing case and the inner side of the flex spline is relatively large, and 2) the mesh between the flex spline and the circular spline does not meet quite well since 3D printed TPU shows slightly lower manufacture resolution than ABS.

4. CONCLUSION

A novel design of a MRI compatible pneumatic motor based on strain wave harmonic mechanism is proposed in this paper, which features few as two inputs, continuous and back-drivable motion outputs, and fast additively manufacture ability (22 components in total). An integrated MRI-compatible speed sensor is designed that provides a pre-aligned click-on/off option for easy installation. Detailed design methods and motor performance tests are presented, offering a new actuation method for the community to actuate various surgical robotic platforms.

Future work includes further design optimization as the proposed MRI compatible harmonic driven pneumatic motor prototype is noticed to have slightly large friction torque compared with other turbine/fan based pneumatic motor. Also, motor performance tests covering larger operating conditions, bandwidth tests for various gear-down ratios and with different lengths of air transmission hoses should be tested in the future to meet a range of practical requirements.

5. REFERENCES

[1] T. Peters and K. Cleary, Image-guided interventions: technology and applications. *Springer Science & Business Media*, 2008.
[2] A. Standard, “F2503. standard practice for marking medical devices and other items for safety in the magnetic resonance environment,” *ASTM International*, West Conshohocken, PA, 2013.
[3] F. G. Shellock, T. O. Woods, and J. V. Crues III, “Mr labelling information for implants and devices: explanation of terminology,” pp. 26–30, 2009.
[4] Q. Xiao, R. Monfaredi, M. Musa, K. Cleary, and Y. Chen, “Mrconditional actuations: A review,” *Annals of Biomedical Engineering*, pp. 1–27, 2020.
[5] Z. Dong, Z. Guo, K.-H. Lee, G. Fang, W. L. Tang, H.-C. Chang, D. T. M. Chan, and K.-W. Kwok, “High-performance continuous hydraulic motor for mr safe robotic teleoperation,” *IEEE Robotics and Automation Letters*, vol. 4, no. 2, pp. 1964–1971, 2019.

[6] A. Bruyas, F. Geiskopf, L. Meylheuc, and P. Renaud, “Combining multi-material rapid prototyping and pseudo-rigid body modeling for a new compliant mechanism,” in *2014 IEEE International Conference on Robotics and Automation (ICRA)*. IEEE, 2014, pp. 3390–3396.

[7] N. Burkhard, S. Frishman, A. Gruebele, J. P. Whitney, R. Goldman, B. Daniel, and M. Cutkosky, “A rolling-diaphragm hydrostatic transmission for remote mr-guided needle insertion,” in *2017 IEEE international conference on robotics and automation (ICRA)*. IEEE, 2017, pp. 1148–1153.

[8] M. Ho and J. P. Desai, “Characterization of sma actuator for applications in robotic neurosurgery,” in *2009 Annual International Conference of the IEEE Engineering in Medicine and Biology Society*. IEEE, 2009, pp. 6856–6859.

[9] S. Hao, A. Camilo, G. A. Cole, H. Nobuhiko, C. M. Tempany, and G. S. Fischer, “High-field mri-compatible needle placement robot for prostate interventions,” *Studies in Health Technology and Informatics*, vol. 163, p. 623, 2011.

[10] R. A. Lathrop, D. C. Rucker, and R. J. Webster, “Guidance of a steerable cannula robot in soft tissue using preoperative imaging and conoscopic surface contour sensing,” in *2010 IEEE International Conference on Robotics and Automation*. IEEE, 2010, pp. 5601–5606.

[11] D.Wu, G. Li, N. Patel, J. Yan, R. Monfaredi, K. Cleary, and I. Iordachita, “ Remotely actuated needle driving device for mri-guided percutaneous interventions,” in *2019 International Symposium on Medical Robotics (ISMR)*. IEEE, 2019, pp. 1–7.

[12] Y. M. Senturk and V. Patoglu, “Design and control of an mri compatible series elastic actuator,” in *2016 IEEE international conference on robotics and biomimetics (ROBIO)*. IEEE, 2016, pp. 1473–1479.

[13] Y. Chen, I. Godage, H. Su, A. Song, and H. Yu, “Stereotactic systems for mri-guided neurosurgeries: a state-of-the-art review,” *Annals of Biomedical Engineering*, vol. 47, no. 2, pp. 335–353, 2019.

[14] C. Nimsky, O. Ganslandt, B. Von Keller, J. Romstock, and R. Fahlbusch, “Intraoperative high-field-strength mr imaging: implementation and experience in 200 patients,” *Radiology*, vol. 233, no. 1, pp. 67–78, 2004.

[15] Y. Chen, S. Xu, A. Squires, R. Seifabadi, I. B. Turkbey, P. A. Pinto, P. Choyke, B. Wood, and Z. T. H. Tse, “Mri-guided robotically assisted focal laser ablation of the prostate using canine cadavers,” *IEEE Transactions on Biomedical Engineering*, vol. 65, no. 7, pp. 1434–1442, 2017.

[16] Y. Chen, I. S. Godage, Z. T. H. Tse, R. J. Webster, and E. J. Barth, “Characterization and control of a pneumatic motor for mr-conditional robotic applications,” *IEEE/ASME Transactions on Mechatronics*, vol. 22, no. 6, pp. 2780–2789, 2017.

[17] Y. Chen, K.-W. Kwok, and Z. T. H. Tse, “An mr-conditional high-torque pneumatic stepper motor for mri-guided and robot-assisted intervention,” *Annals of Biomedical Engineering*, vol. 42, no. 9, pp. 1823–1833, 2014.

[18] G. S. Fischer, I. Iordachita, C. Csoma, J. Tokuda, S. P. DiMaio, C. M. Tempany, N. Hata, and G. Fichtinger, “Mri-compatible pneumatic robot for transperineal prostate needle placement,” *IEEE/ASME Transactions on Mechatronics*, vol. 13, no. 3, pp. 295–305, 2008.

[19] F. S. Farimani and S. Misra, “Introducing pneuact: parametricallydesigned mri-compatible pneumatic stepper actuator,” in *2018 IEEE International Conference on Robotics and Automation (ICRA)*. IEEE, 2018, pp. 200–205.

[20] H. Sajima, H. Kamiuchi, K. Kuwana, T. Dohi, and K. Masamune, “Mrsafe pneumatic rotation stepping actuator,” *Journal of Robotics and Mechatronics*, vol. 24, no. 5, pp. 820–827, 2012.

[21] Y. Chen, C. D. Mershon, and Z. T. H. Tse, “A 10-mm mr-conditional unidirectional pneumatic stepper motor,” *IEEE/ASME Transactions on Mechatronics*, vol. 20, no. 2, pp. 782–788, 2014.

[22] D. Stoianovici, A. Patriciu, D. Petrisor, D. Mazilu, and L. Kavoussi, “A new type of motor: pneumatic step motor,” *IEEE/ASME Transactions on Mechatronics*, vol. 12, no. 1, pp. 98–106, 2007.

[23] V. Groenhuis, F. J. Siepel, and S. Stramigioli, “Dual-speed mr safe pneumatic stepper motors.” in *Robotics: Science and Systems*, 2018.

[24] D. B. Comber, J. E. Slightam, V. R. Gervasi, J. S. Neimat, and E. J. Barth, “Design, additive manufacture, and control of a pneumatic mrcompatible needle driver,” *IEEE Transactions on Robotics*, vol. 32, no. 1, pp. 138–149, 2016.

[25] J. Erlach, “Pelton turbine,” Aug. 21 1990, US Patent 4,950,130.

[26] M. Turkseven and J. Ueda, “An asymptotically stable pressure observer based on load and displacement sensing for pneumatic actuators with long transmission lines,” *IEEE/ASME Transactions on Mechatronics*, vol. 22, no. 2, pp. 681–692, 2016.

Biographies

Mengtang Li received the B.S. degree with honor in Astronautics Engineering from Northwestern Polytechnical University, Xi’an, China, in 2014, the M.S. degree in Electrical Engineering and the Ph.D. degree in Mechanical Engineering from Vanderbilt University, Nashville, TN, USA, in 2016 and 2020, respectively. Dr. Li was a visiting scholar in Sarver Heart Center, School of Medicine, University of Arizona during 2018 to 2020. He is currently an Assistant Professor in School of Intelligent Systems Engineering in Sun Yat-Sen University, Shenzhen, China. His research interests include fluid powered soft robotic system design and control, mechanical circulatory support device (total artificial heart, ventricular assist device) design, mobile unmanned robots/vehicles/aircrafts control.

Jing Zhang is currently pursuing her B.S. degree with School of Intelligent Systems Engineering, Shenzhen Campus of Sun Yat-Sen University, Shenzhen, China. Her research interests include modelling and control of surgical robots.

Xiyun Wu is currently pursuing her B.S. degree with School of Intelligent Systems Engineering, Shenzhen Campus of Sun Yat-Sen University, Shenzhen, China. Her research interests include modelling and control of surgical robots.

Jieting Yuan is currently pursuing her B.S. degree with School of Intelligent Systems Engineering, Shenzhen Campus of Sun Yat-Sen University, Shenzhen, China. Her research interests include machine learning and deep learning.

Xiyu Wang is currently pursuing the B.S. degree with School of Intelligent Systems Engineering, Shenzhen Campus of Sun Yat- sen University, Shenzhen, China.
Her research interests are in robotics and machine learning.

Yongyin Ye is currently pursuing the B.S. degree with School of Intelligent Systems Engineering, Shenzhen Campus of Sun Yat-Sen University, Shenzhen, China. Her research interests are related with Neural Network Learning and Applications of parallel robots and Intelligent Control.

Beichen Ding received his Ph.D. in Mechanical Engineering from the University of Bath, UK, in 2019. He is currently an Associate Professor in the School of Intelligent Systems Engineering, Sun Yat-sen University, China.